ELECTROCHEMISTRY

Fixture-free omnidirectional prestretching fabrication and integration of crumpled in-plane micro-supercapacitors

Ying Wang[1], Yang Zhao[1]*, Yuyang Han[1], Xiangyang Li[1], Chunlong Dai[1], Xinqun Zhang[1], Xuting Jin[1], Changxiang Shao[1], Bing Lu[1], Chengzhi Wang[1], Huhu Cheng[2], Feng Liu[3]*, Liangti Qu[2]*

Multidimensional folded structures with elasticity could provide spatial charge storage capability and shape adaptability for micro-supercapacitors (MSCs). Here, highly crumpled in-plane MSCs with superior conformality are fabricated in situ and integrated by a fixture-free omnidirectional elastic contraction strategy. Using carbon nanotube microelectrodes, a single crumpled MSC holds an ultrahigh volumetric capacitance of 9.3 F cm^{-3}, and its total areal capacitance is 45 times greater than the initial state. Experimental and theoretical simulation methods indicate that strain-induced improvements of adsorption energy and conductance for crumpled microelectrodes are responsible for the prominent enhancement of electrochemical performance. With outstanding morphological randomicity, the integrated devices can serve as smart coatings in moving robots, withstanding extreme mechanical deformations. Notably, integration on a spherical surface is possible by using a spherical mask, in which a small area of the microdevice array (3.9 cm^2) can produce a high output voltage of 100 V.

INTRODUCTION

Miniaturize energy storage devices have become increasingly important for the next generation of renewable energy, enabling a compatibility of energy supply and microelectronics industry that is unattainable in traditional bulk power supply equipment (*1*). Micro-supercapacitors (MSCs), especially in-plane forms, have become one of the most competitive candidates, which is not only for their miniature size, fast charge-discharge ability, long cycle life, and robust security (*2*, *3*) but also for the separator-free configuration that can meet the multidirectional rapid ion diffusion and avoidance of short circuit. Recent empirical observations in MSCs revealed that the principal affecting charge storage capability can also be dictated by microstructural morphologies besides material because of the finite spatial confinement and the resulting prominent interface effect in microelectrodes, which mainly relied on reasonable structural design and fabrication protocols. Current well-developed preparation ways of two-dimensional (2D) in-plane microelectrodes are to construct patterned electrode films on a planar substrate by screen printing, spray-ink printing, electrodeposition, filtration, laser direct writing, etc. However, because of the limitation of space and device size, the electrochemical capacity is still unsatisfactory for practical use. Even though 3D in-plane MSCs were developed to make up for the shortage of capacitance in area, the accumulated electrode thickness greatly impedes the preparation precision and leads to a sluggish kinetic behavior for MSCs.

For the optimization of planar MSC processing technology, it is necessary to consider how to expose more electrode materials to the electrolyte as much as possible on a microscaled area. Recently, prestretching strategy has been widely studied in stretchable devices (*4*–*13*), wherein the material film covered on the uniaxial or biaxial prestretched elastomer is extruded and deformed after the substrate relaxation, resulting in a tightly packed crumples. The experiment results show that the existence of abundant compact folded structures could provide more exposed surface area in a same space than that of block structures. Therefore, we attempt to combine the screen-printing method with the prestretching strategy (Fig. 1A), aiming to produce active electrode surfaces tightly packed within a narrow patterned area. Without complex fixtures, a commercial latex balloon is chosen as the omnidirectional prestretched elastic substrate in the state of inflation, which makes up for the nonuniformity of the stretching direction in the traditional prestretched systems. Then, carbon nanotube (CNT) ink with superior mechanical property and high electrical conductivity is used as the suitable candidate of the compressible electrode materials (*14*). By scraping the CNT ink on the mask coated on the balloon surface, the patterned electrodes were then formed via removing the mask (Fig. 1A). It is worth mentioning that the expanded balloon can provide sufficient support for the attachment of the mask and electrode materials, effectively reducing the difficulty of operation. After precoating a layer gel electrolyte, the crumpled MSC was obtained as the balloon deflates, realizing the one-step transformation from macro-operation to microdevice generation. Furthermore, the microdevices produced by omnidirectional contraction stress have a remarkable conformality, which can achieve the diversified design.

As a result, a single crumpled MSC exhibits a small area of ~0.02 cm^2 and a high areal capacitance of 13.5 mF cm^{-2}, which are nearly 13 times less and 45 times greater than the initial state. Meanwhile, it also has a high volumetric capacitance of 9.3 F cm^{-3} (about 3.6 times higher than the initial state) superior to the CNT-based microdevices reported previously. The mechanism of performance enhancement for the crumpled MSC is further proposed from the experiments and theoretical simulations. Resulting that the compact crumple structure improves the conductance and reduces the

[1]Key Laboratory of Cluster Science, Ministry of Education of China, Beijing, Key Laboratory of Photoelectronic/Electrophotonic Conversion Materials, School of Chemistry and Chemical Engineering, Beijing Institute of Technology, Beijing 100081, P. R. China. [2]Key Laboratory of Organic Optoelectronics and Molecular Engineering of Ministry of Education, Department of Chemistry, Tsinghua University, Beijing 100084, P. R. China. [3]State Key Laboratory of Nonlinear Mechanics, Institute of Mechanics, Chinese Academy of Sciences, Beijing 100190, P. R. China.
*Corresponding author. Email: lqu@mail.tsinghua.edu.cn (L.Q.); yzhao@bit.edu.cn (Y.Z.); liufeng@imech.ac.cn (F.L.)

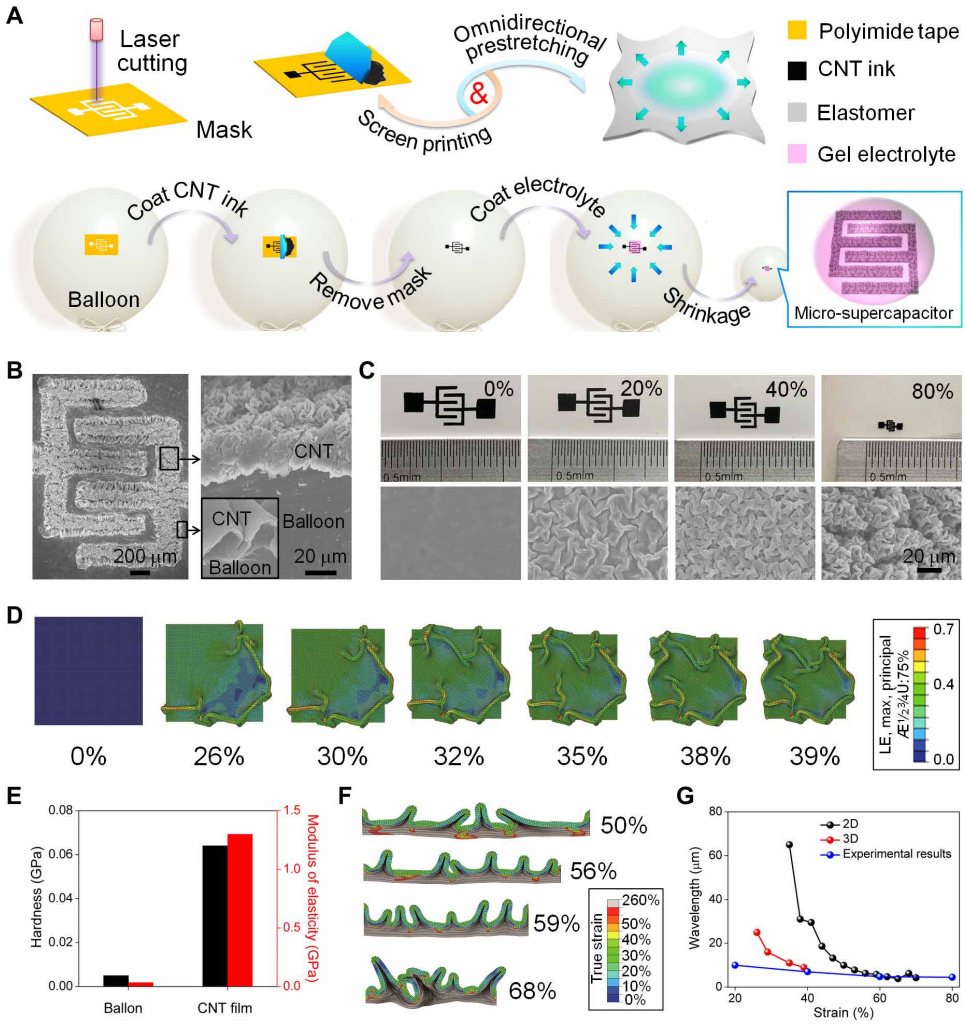

Fig. 1. Fabrication and structural characterization of MSCs. (**A**) Schematic illustration of fabricating the interdigital microelectrodes and strain-induced MSC. (**B**) Top view and cross-sectional scanning electron microscopy (SEM) images of crumpled CNT film microelectrodes. (**C**) Optical and SEM images of microelectrodes under different strains. (**D**) Maximum principal strain distribution evolution with respect to compressive strains. (**E**) Nanohardness and elastic modulus of the samples measured by nanoindentation. (**F**) Finite element method (FEM) calculation results of CNT film structure with its substrate (the balloon) under different compression strains; the wrinkling behavior is triggered with its amplitude and periodicity gradually evolving. (**G**) Wavelength of crumpled carbon nanotube (CNT) film with respect to compressive strain.

ions adsorption energy of CNT films, thus providing more effective active surface areas and enhanced electrochemical activity. As expected, this enhancement behavior is also confirmed by testing in various electrolytes. With the strategy, a minimum microdevice with 0.1 mm^2 is achieved, in which the individual finger width and interelectrode gap are only 44 and 20 μm, respectively. This is the smallest device size that can be obtained by using the screen-printing method without sophisticated processing.

Benefiting from the elastic balloon substrate, the large-scaled spherical integrated microdevices were readily developed by using a customized spherical mask, which provides a breakthrough idea for machining challenging curved devices. A set of microdevice arrays with only a small area of 3.9 cm^2 could produce a high output voltage of 100 V. Afterward, the microdevices with flexible and mechanical stability can sustain bend, knead, prod, and knot deformations, enabling the applications in wearable, flyable, and underwater power systems. This is in marked contrast to other miniature flexible energy storage devices. These findings open a pathway to a wide range of design thoughts on the robust, cambered, and wearable miniature energy storage devices in smart application possibilities.

RESULTS

Fabrication and characterization of crumpled in-plane MSCs

The schematic diagrams of the preparation process for MSC are illustrated in Fig. 1A. Here, the prestretching strategy is adopted to attain the desirable microstructured electrodes and microdevice size. To get rid of the cumbersome and uncontrollable prestretching ways, a commercial inflatable balloon that is capable of high stretchability and elasticity is introduced as the prestretching substrate without extra fixture. Using the reversible deformation of the balloon in a wide strain range caused by a simple inflating and deflating operation, we can achieve both micro- or potentially nanoscale structures or patterns. This fabrication process could provide a simple and scalable means to produce simultaneous construction of microelectrodes and internal microstructures across multiple area scales.

It should be pointed out that the mechanical stability and homogeneity of material are required under large deformations, and the inflated balloon can provide an omnidirectional stress during the relaxation process. Considering the outstanding conductive and mechanical abilities (*15*, *16*), CNT is selected as the exemplified electrode material and current collector, which is expected to produce a fully self-adaptable energy storage system. To verify the feasibility of this viewpoint, we first prepared CNT ink and achieved the expected effect (fig. S1). For the following exploration, the similar commercial aqueous CNT ink was used to shorten the device fabrication period (related characterizations can be seen in fig. S2).

To construct the MSC, the interdigital electrode mask made of polyimide (PI) tape engraved by an ultraviolet laser cutting system was firstly attached on the rubbed surface of an inflatable balloon (400% prestretch), followed by evenly coating with CNT ink (Fig. 1A). The optimum CNT ink concentration in the MSC fabrication is discussed in detail in fig. S3. Then, the interdigital electrodes were obtained by removing the excess CNT materials with a scraper. The total amount of CNTs depends on the area and thickness of the patterned PI masks (see details in section S1.3). After completely drying at room temperature and removing the mask, the confined CNT film interdigital electrodes with uniform distribution were formed and tightly combined with the inflated balloon substrate by electrostatic and cementing interaction (see fig. S4 and section S2.3) (*17*). To ensure adequate contact between microelectrodes and electrolytes, an appropriate amount of semisolid gel electrolytes was coated on the microelectrodes during balloon expansion, whereas the crumpled MSC can be handily obtained by a facile one-step deflating process (Fig. 1A). From the scanning electron microscopy (SEM) images in Fig. 1B, the microelectrode films display uniform 3D crumpled microstructures induced by a high contraction strain of 80%, while the 2D folded microstructures can be observed at the electrode edges because of the edge effect (inset in Fig. 1B).

To investigate the evolution of electrode microstructure and properties with strain, a series of MSCs with regulable sizes were constructed by simply shrinking the balloon to 0, 20, 40, and 80% compress strains (Fig. 1C and fig. S5). As shown in Fig. 1C, the device area decreases from 0.26 to 0.021 cm^2 with the contraction strain increasing from 0 to 80%, and the microelectrode gap drops sharply from 600 to about 100 μm (Fig. 1B), which may effectively reduce the transport route of electrolyte ions. Correspondingly, the SEM images reveal a smooth surface of the CNT electrodes with 2-μm thickness at 0% strain (Fig. 1D and fig. S6A), in which the folds with large wavelength gradually form under a mild compression strain of 20%, then the wavelength becomes smaller but denser at a high compaction state of 80% strain. Moreover, the tightly packed CNT films with negligible damage at the bent section can be observed in the SEM images of microelectrodes even at high strain (80% strain; Fig. 1C). Meanwhile, the amplitude of the folds increases as the wavelength decreases (fig. S6, B to D), which may provide more spatial active sites.

As the balloon deflates, the compression stress and strain suffered by CNT electrodes were further tracked by establishing a 3D Neo-Hookean bilayer model based on biaxial compression strains (Fig. 1D). Both evolution of maximum principal strain and von Mises stress strain distributions with respect to compressive strain is shown in Fig. 1D and fig. S7. With compressive strain increases, the fold occurs around 26%. This 2D fold phenomenon is essentially originally from the mismatch of mechanical properties between the CNT film and the balloon substrate (Fig. 1E and fig. S8) (*18*), which is a typical form of mechanical instability. Since stress and strain are concentrated at the folds, the surrounding stress and strain are alleviated, which in turn reduces total elastic energy. The fold geometrical feature obtained in our finite element method (FEM) is quite similar to experimental ones (Fig. 1C) suggesting the validity of Neo-Hookean bilayer in 3D model. Combining experimental and FEM results (Fig. 1, C, F, and G), it could also be seen that the wrinkling periodically decreases in wavelength and increases in amplitude as the balloon substrate gradually shrinks (figs. S9 and S10), signifying that the number of derived folds increases continuously at high strain and may provide more opportunities for charge storage.

Electrochemical characteristics of MSCs

The electrochemical behaviors of the obtained MSCs at different strains are investigated in 1 M PVP-H_2SO_4 gel electrolyte. Before the exploration, the interaction between the balloon substrate and the electrolyte was evaluated through x-ray diffraction spectra and cyclic voltammetry (CV) curves of the crumpled MSC. As a result, the balloon covered with the electrolyte for 12 hours has no excess characteristic peaks (fig. S11A), while the CV curve of the MSC after dropping electrolyte for 12 hours shows only a small increase in capacitance, and no other electrochemical behaviors can be seen compared with the initial state, demonstrating the considerable stability and feasibility of this energy storage system (fig. S11B). As displayed in Fig. 2A, CV curves of all devices exhibit typical electric double layer behaviors (50 mV s^{-1}; Fig. 2A), in which the current increases significantly as the strain increases (fig. S12). In particular, the MSC at 80% strain presents a satisfactory rectangular shape and the largest response current among its counterparts, reflecting the enhanced charge storage capability and rapid electron transfer within the microelectrodes (*19*). A similar phenomenon also goes to the galvanostatic charge-discharge (GCD) curves in Fig. 2B. At current density of 0.072 A cm^{-3}, all the devices show almost symmetrical charge-discharge behaviors, and their variation trend with strain is consistent with CV curves. The voltage drop by current (IR drop) of GCD curves become negligible as the strain increases (Fig. 2B), demonstrating the obvious improvement of charge utilization and effective voltage as the formation of featured crumpled structures in the reduction of device size. For the optimal MSC at 80% strain, its GCD curves at current densities from 0.036 to 0.72 A cm^{-3} are shown in Fig. 2C. The discharge time decreases appropriately with the increasing current densities, resulting in satisfactory rate capabilities (Fig. 2D). Last, the strain induces a high volume-specific capacitance of 9.3 F cm^{-3} (at 0.036 A cm^{-3}) for the MSC at 80% strain, nearly 3.6 times greater than that of the initial state (0% strain; Fig. 2E). Meanwhile, the MSC at 80% strain also has a high area-specific capacitance of 13.5 mF cm^{-2}, even 45 times greater than that of 0% strain (0.3 mF cm^{-2}; fig. S13). The remarkable performance of prepared MSC is quite competitive in CNT-based MSCs reported previously, even higher than CNT composites–based MSCs (Fig. 2F and tables S1 and S2) (*20*–*34*).

Electrochemical impedance spectroscopy was further carried out to comprehend the kinetics of ion transport. The Nyquist plot for the MSC at 0% strain (Fig. 2G) displays obvious Warburg region accounting for sluggish ion transport. With the increase in strain, both charge transfer resistance (R_{ct}) and solution resistance (R_s) get smaller, and the Warburg region gradually disappears, which can be attributed to accelerated ion diffusion between the electrode material and the electrolyte in the featured microstructures. In addition,

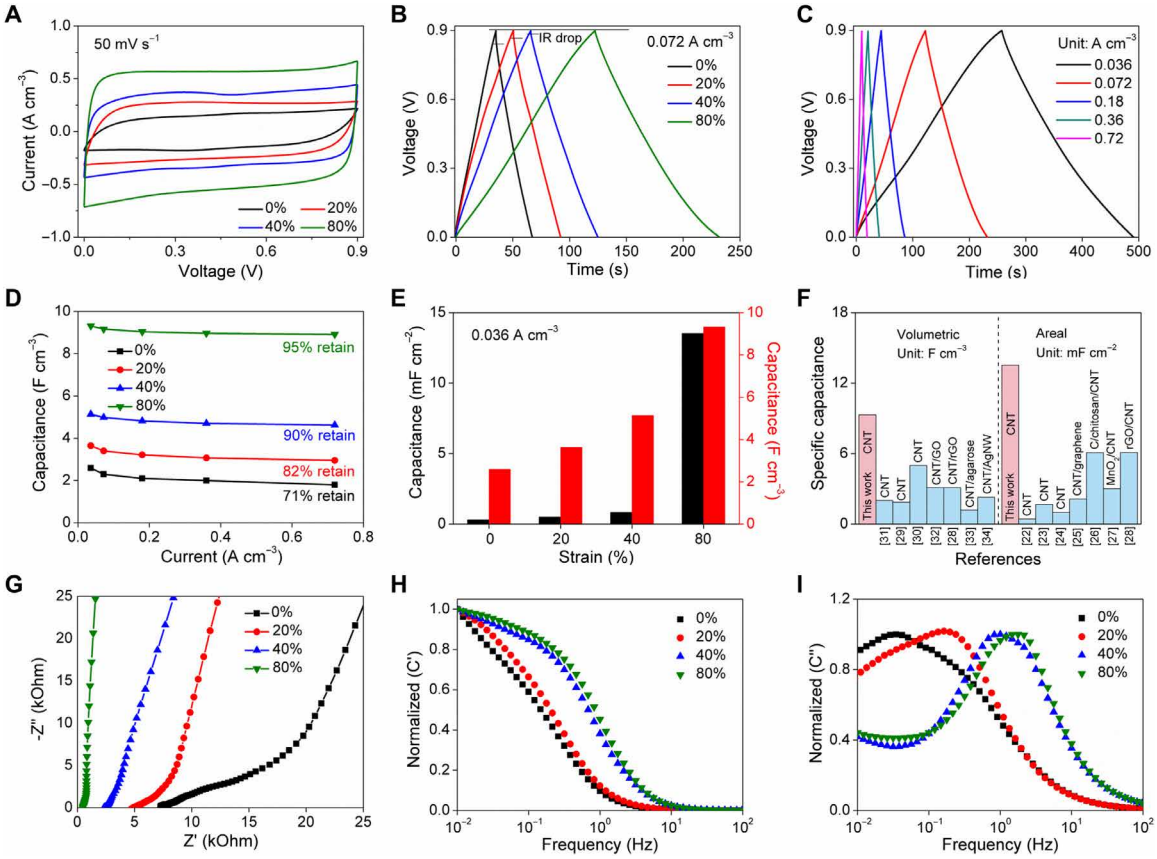

Fig. 2. Electrochemical performances of prepared MSCs. (**A**) CV and (**B**) galvanostatic charge-discharge (GCD) curves of MSCs under various strains. (**C**) GCD curves of the MSC at 80% strain. (**D**) Rate capacities of the MSCs at different strains. (**E**) Device area and electrode volume–specific capacitance comparison under different strains. (**F**) Electrode volume– and device area–specific capacitance comparison of different CNT-based MSCs. (**G**) Nyquist plots and normalized imaginary part capacitance of different devices. Normalized (**H**) real and (**I**) imaginary part capacitance.

the almost vertical line in the low frequency for the MSC at 80% strain is ascribed to the ideal capacitive behavior. Bode plot, the real and imaginary part capacitance (C' and C'') versus frequency, is depicted in Fig. 2 (H and I). The real capacitance decreases at high frequencies, meaning the transition from capacitance response to resistance response. Compared with 0% strain, the obvious plateau can be found in the MSC at 80%, illustrating its wider capacitance response and better capacitive behavior (Fig. 2H). At the same time, imaginary capacitance is associated with some irreversible consumption process, and short relaxation time constant ($\tau_0 = 1/f$) calculated in C'' of 80% strain MSC is further supported by its rapid transportation of charge and fast electrode polarization (*35*–*37*), leading to the enhanced ion diffusion (fig. S14) (*38*) and energy/power densities (0.38 mW cm^{-2}/1.4 mWh cm^{-2}; fig. S15A). Then, the MSC (80% strain) reaches a considerable capacitance retention of 93% and a high coulombic efficiency of ~95% after 12,000 cycles (fig. S15B).

Mechanism of electrochemical performance enhancement

Why does the strain-induced MSC make a robust electrochemical capacity? It is observed that the change of device size and the generation of crumpled structure in microelectrodes are the two strain-induced characteristics, which can be considered as the two main reasons for improving the performance. To quantify the effects of these two factors, three stacked in-plane devices in three specific areas of the devices at three different strains (20, 40, and 80%) were fabricated, and the similar mass of each device was adjusted by the thickness of microelectrodes (fig. S16). As shown in Fig. 3A, it can be seen that the device capacitances of stacking-20%, stacking-40%, and stacking-80% have 123, 150, and 200% improvement in comparison with the initial device (at 0% strain). Without crumpled structures, the appropriate capacitance enhancement is mainly due to the size minification of stacked devices, which effectively reduces the charge transmission distance and resistance. In contrast, the asymmetrical GCD curves can be seen in the stacked in-plane device at small size (fig. S17A), and the accumulated electrode thickness may weaken the reversibility and kinetics of the electrochemical reaction (fig. S17, B and C). On the basis of the above investigation, the contribution ratio of device size change and derived crumpled structure in strain-induced MSC can be approximately inferred in Fig. 3B. As the strain increases, the contribution of crumpled structure increases from 42 to 60%, suggesting that the formed microstructure is beneficial for charge storage but has received little attention. Therefore, the influence of crumpled structure on electrochemical performance will be analyzed in detail by combining theoretical simulations and experiments.

Apart from the factor of device size change, the corresponding microstructure evolution of the CNT film under strain could be the

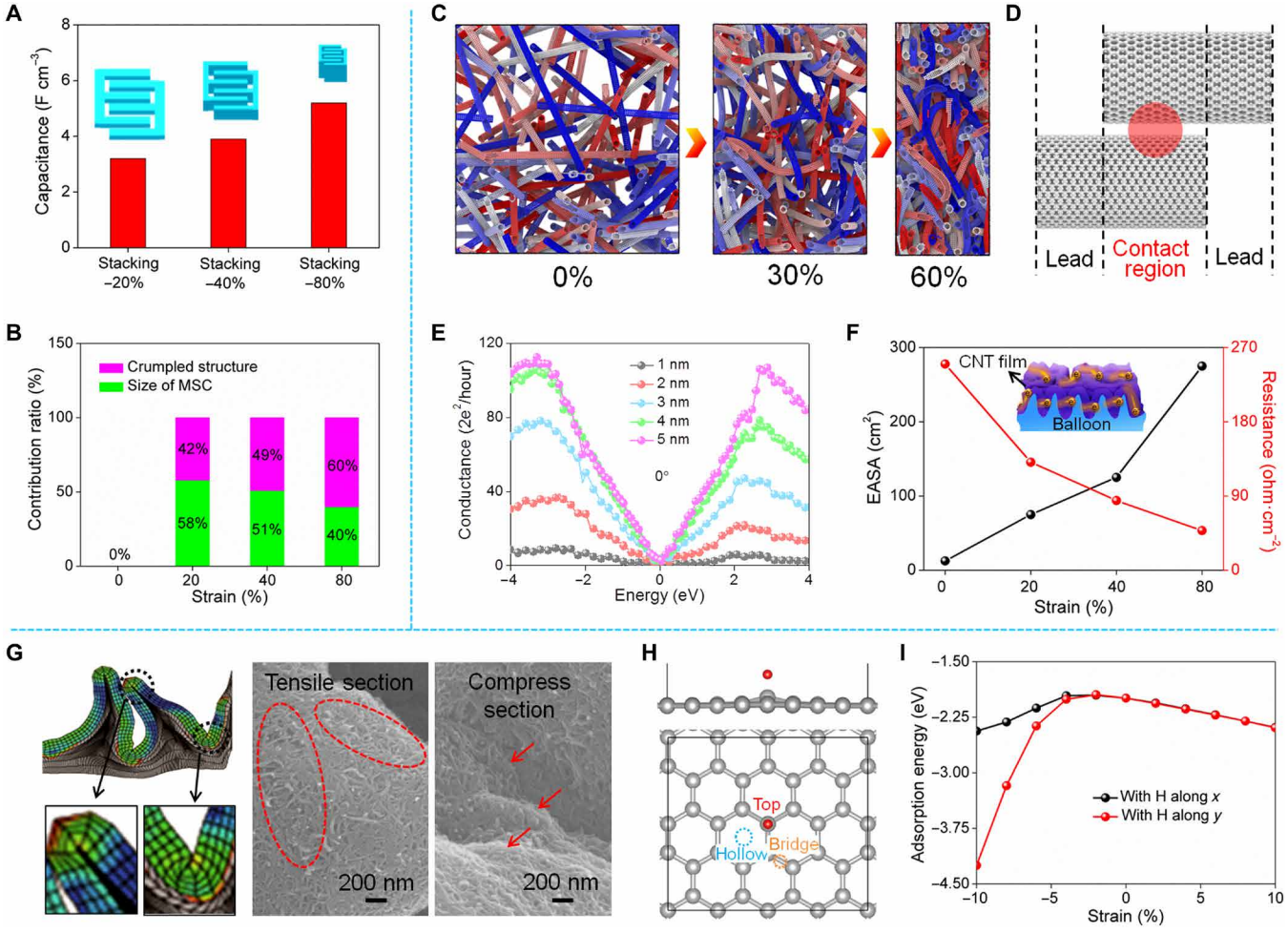

Fig. 3. Mechanism of electrochemical performance enhancement. (**A**) Capacitances of the three devices measured at current density of 0.036 A cm^{-3}. (**B**) Contribution of crumpled microstructures and device sizes to MSC capacitance enhancement under different strains. (**C**) Molecular dynamics simulation of uncovered CNT microstructure evolution under biaxial compression. (**D**) Schematic diagram of transport model. (**E**) Evolution of the contact conductance of the lattice twist angle of 0°. (**F**) Effective active surface areas (EASA) and resistance of the CNT film electrodes at different strains. (**G**) FEM calculation results of 70% strain CNT film structure with its substrate (the balloon) and high-resolution SEM images of bending the CNT film at tensile and compress sites. (**H**) Unit cell of graphene/H (Gr/H) system, and three hydrogen adhesion sites, i.e., top, bridge, and hollow sites, are marked with red, orange, and blue, respectively. (**I**) Under the uniaxial strain along the armchair and zigzag directions, the adsorption energies of the Gr/H system were calculated with $E_b = E_{Gr\text{-}H} - E_{Gr} - E_H$.

key to understand its greatly improved electrochemical activities. First, the intrinsic resistance change of the CNT film under compression strain is analyzed by coarse-grained molecular dynamics (MD) simulation (Fig. 3C and fig. S18) (*39*, *40*) and mesoscopic transport theory (Fig. 3, D and E, and fig. S19) (*41*–*44*). As the MD result is shown in Fig. 3C, with compression increasing, CNTs pack more closely, and bending deformation of individual CNT becomes more severe (fig. S19A), which is consistent with the corresponding SEM images and ultraviolet-visible (UV-vis) diffuse absorption (figs. S20 and S21). Close packing and bending deformation of CNT foams are directly related to their electrical conduction and adhesion properties (*45*), respectively; both, which influence the improved capacitance, will be carefully discussed with MD simulation. Subsequently, the transport model is established (see section S2.12 for details) to further study the contact conductance between two touched CNTs (Fig. 3D). The energy-resolved contact conductance with the twist lattice angle from 0° to 30° is calculated (Fig. 3E and fig. S19, C to F). As a result, with the increase in average contact area and region number between CNTs (fig. S19B), the contact conductance amplitude increases and provides more opportunities for CNTs to touch with each other with different twist lattice angles. Thus, a smaller bandgap could be expected, which well reproduces the experimental measurement qualitatively (fig. S21C). Thanks to the improvement of the contact conductance of CNTs, the electrochemical activity and charge storage capability of the CNT film become stronger with the increased strain. Specifically, the electrochemical activity (fig. S22, detailed test in the Supplementary Materials) and effective active surface area (Fig. 3F and fig. S23) of CNT film electrodes were evaluated in a three-electrode system, both of which revealed sharply enhanced behaviors with the increasing strain. In particular, the increase in the active surface area of the electrode highly depends on the decrease in resistance to the ascending strain (Fig. 3F and fig. S24). Clearly, the strain-derived compact fold structures in the CNT film create many contact points, which may

provide more and shorter charge transport paths, effectively alleviating the film resistance and energy loss (Fig. 3F, inset).

In addition, the capacitance of the device is also proportional to the generated fold number, and the strain is mainly concentrated in the fold tip region of the crumpled CNT film because of the local extreme bending deformation (FEM in Fig. 3G); thus, the strain-induced electrochemical performance enhancement may exist. Under macroscopic contraction, the strain distribution on the surface of the CNT film is heterogeneous and could change from compressive to tensile. The CNTs with tensile and compress states in the peaks and valleys of the bent CNT film can be seen in high-resolution SEM images (Fig. 3G), which is consistent with the FEM results. To verify this point of view, the issue of hydrogen atom adhesion on CNTs is also considered through first principles calculation (Fig. 3H and fig. S25) (*46*–*48*). In Fig. 3H, three possible hydrogen atom adhesion configurations are shown, where hydrogen atom position is set to top, bridge, and hollow sites, respectively. It is interesting to find out that regardless of being under tensile or compressive strain, the adsorption energy of the Gr/H system generally decreases, concluding that deformation could promote the adhesion of hydrogen atom to graphene or CNTs (Fig. 3I; see section S2.15), which can further guarantee the promotion of charge storage capacity.

Universality of prepared microdevices

To verify the reliability of the above investigations, the electrochemical tests of this strain-induced MSC were performed in a series of aqueous gel electrolytes ranging from acidic to alkaline. As shown in Fig. 4A and fig. S26, the strain-induced crumpled MSC exhibits the promotive adsorption and storage capacities for various zwitterion under different acid-base conditions, illustrating that the improved electrochemical performance is associated with device structures. In addition, the negligible influence of balloon curvature radius on MSC performance is also demonstrated in Fig. 4B and fig. S27, where the balloon only acts as an elastic substrate. By this strategy, an ultrasmall-sized energy storage device with high precision was obtained, far smaller than those ones by traditional printing/template methods (*49*–*51*). In detail, the electrode mask size was reduced 16 times within the allowable range to fabricate the ultrasmall supercapacitors. Meanwhile, to ensure the high resolution of the device, the concentration of the CNT ink was also reduced by eight times

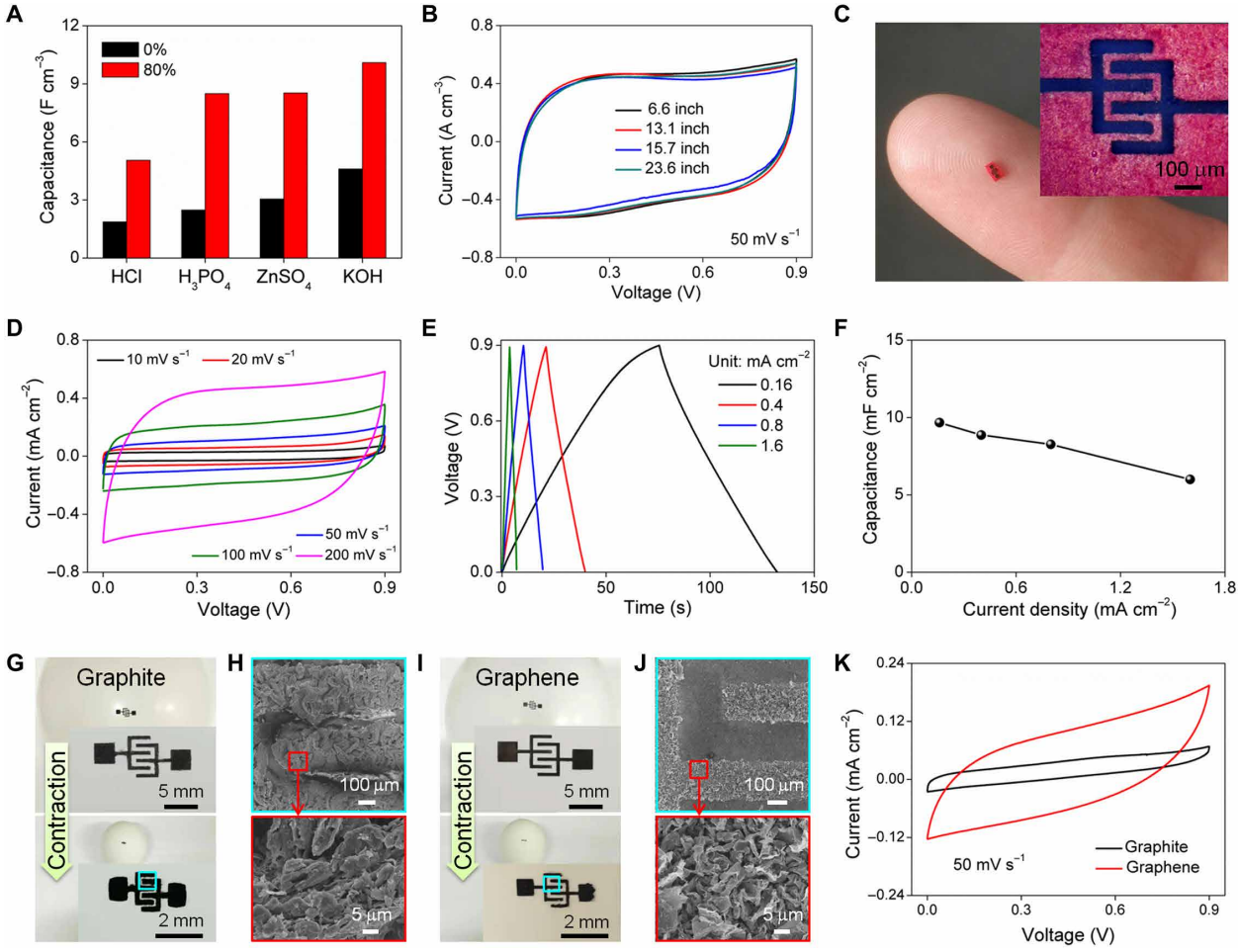

Fig. 4. Universality of the strain-induced in-plane MSCs. (**A**) Specific capacitances of the devices with various gel electrolytes (current density of 0.036 A cm^{-3} in 1 M HCl, H_3PO_4, and $ZnSO_4$ gel electrolyte systems; current density of 0.36 A cm^{-3} in 1 M KOH gel electrolyte). (**B**) CV curves of crumpled MSCs with the balloon substrates of different radii. (**C**) Optical images of the micrometer-scale MSC. (**D**) CV, (**E**) GCD curves, and (**F**) rate capacity of micrometer-scale MSC. Photographs of (**G**) graphite- and (**I**) graphene-based interdigital electrodes before and after contraction. SEM images of (**H**) graphite- and (**J**) graphene-based crumpled microelectrodes. (**K**) CV curves of the two crumpled MSCs.

to avoid the overflow of heavy electrode material and its limitation of balloon shrinkage. Eventually, the whole microdevice with an area of ~0.1 mm^2 (297 μm in width and 419 μm in height) was obtained, in which the individual finger width and interelectrode gap are only 44 and 20 μm, respectively, even less than the width of a fingerprint stripe (Fig. 4C). After measuring in 1 M H_2SO_4 gel electrolyte, the stable electrochemical performance is described by the CV (Fig. 4D) and GCD (Fig. 4E) curves, revealing a high areal capacitance of 9.7 mF cm^{-2} at current density of 0.16 mA cm^{-2} (Fig. 4F). The universality of the proposed fabrication strategy is important to apply in the field of stretchable and wearable electronics. Apart from 1D CNT electrode system, 2D graphite and graphene aqueous inks with appropriate concentration were also attempted as raw materials of electrodes for elastic crumpled MSCs. As the photographs shown in Fig. 4 (G and I), the contracted microelectrodes of graphite and graphene with excellent conformality largely retain the interdigital shape of the initial electrodes. Meanwhile, both the graphite and graphene microelectrodes show crumpled microstructure without short-circuit behavior (Fig. 4, H and J) and can work normally after being assembled into MSCs (Fig. 4K). The above experimental results show that both the proposed fabrication method of crumpled MSCs and their improved performance by optimizing microdevice structures are universal.

Programmable and integrated crumpled MSCs with superior conformality

By virtue of the peculiarity of omnidirectional deformability of balloon substrate, this strategy could allow the facile construction and integration of MSCs with diversity. The microelectrodes can be prefabricated into various configurations on the surface of an inflated balloon, which will remain the predesigned patterns once the balloon contracts (e.g., 80% strain). On the one hand, the CNT microelectrodes with multiple patterns can be achieved through laser programming of various patterned masks, in which SEM characterizations reveal the consistent featured folding microstructures caused by the omnidirectional compression strategy (Fig. 5, A to C). With 1 M PVP-H_2SO_4 electrolyte, all of these diverse patterned MSCs display good rate capacities (fig. S28), illustrating strong universality of this fabrication strategy. On the other hand, the MSCs can also be integrated in series or parallel connections in a similar processing way to meet various electrical devices with different energy thresholds (fig. S29A). The shapes of as-formed series or parallel MSC arrays at 80% strain (Fig. 5D and fig. S29B) exhibit almost the same as those of the original devices at 0% strain without any short circuit phenomenon. The electrochemical measurements reveal stable electrochemical performance and ignorable attenuation for integrated MSCs in series or in parallel. Moreover, both the CV and GCD profiles of

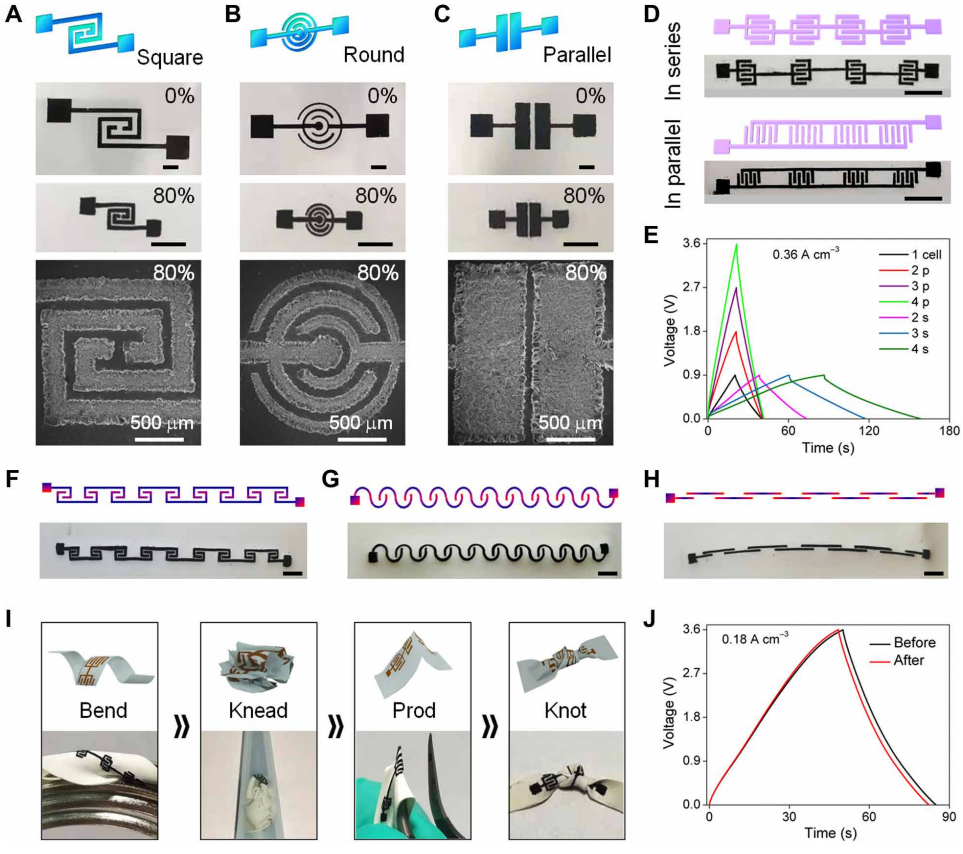

Fig. 5. Conformality and mechanical stability of programmable and integrated MSCs. (**A** to **C**) Digital and SEM images of shape-tailored electrodes at 0 and 80% contraction strains. Scale bars, 2 mm. (**D**) Schematic diagram and digital images of the integrated devices connecting in series and in parallel at 80% compress strain. Scale bars, 2 mm. (**E**) GCD profiles of integrated MSCs with 2 to 4 U connecting in series and in parallel. (**F** to **H**) Digital images of shape-tailored integrated MSCs under 80% strains. Scale bars, 2 mm. (**I**) Integrated MSCs are treated with various mechanical deformations of bend, knead, prod, and knot. (**J**) GCD profiles of the integrated MSC before and after a series of mechanical deformations.

series-connected MSCs exhibit a trend of gradual linear increase in operating voltage (Fig. 5E and fig. S29C), while the current densities in CV curves of parallel-connected MSC also rise steadily under the same voltage window. The discharging time of parallel MSCs with two, three, and four devices in parallels is almost two, three, and four times longer than that of the single unit at the same discharge current density. Notably, the IR drop in both series and parallel devices is inconspicuous (Fig. 5E), which is mainly due to the strain-induced reduction of the whole device size and polarization. As for conformality, the integrated microdevices can be designed as to specific patterns on demand in various application requirements (Fig. 5, F to H, and fig. S30).

On the basis of the intrinsic elasticity of the natural latex balloon substrate, the as-formed MSCs inherit the peculiarity of outstanding flexibility and mechanical strength. As exemplified in Fig. 5I, the integrated MSCs with four individual units in series cut from the balloon substrate can sustain a series of harsh deforming processes, such as bend, knead, prod, and knot. With the severe deformations of MSCs, an inconspicuous decay is observed in the charge-discharge time at the same current density (Fig. 5J), which may be caused by a small amount of shedding of the superficial CNTs and trifling crack generated on the CNT film (fig. S31A). At the same time, the mechanical stability of the individual device was also assessed by repeatedly contracting and expanding the balloon elastic substrate at 60% strain. After 200 cycling tests, the microdevice maintains a relatively steady electrochemical performance with a slight capacitance attenuation (fig. S31B), probably due to a small amount of breakage generated on the electrodes after cycling (fig. S31C). Nevertheless, the expressed flexibility under extreme deformation conditions is far superior to those miniature flexible energy storage devices reported previously, further expanding its applied scope.

Diversified application of integrated MSCs

With the omnidirectional compression process of the balloon, the flexible and mechanically stable MSC array displays a robust tensile capability in multispatial dimensions (fig. S32, A and B). Compared with the previous publications of stretchable energy storage microdevices (table S3) (*52*–*61*), this MSCs connected in series can not only achieve multiaxial deformation but also normally light a red light-emitting diode (LED) at a high strength of 400% deformations (fig. S32C). Electrochemical tests of the integrated microdevices bonded to arbitrary 3D surfaces reveal no obvious change of CV curves (fig. S33, A and B), indicating the strong shape adaptability and tolerance of the MSCs, and the integrated microdevices can even be randomly tucked in crevices of a building model to light a string of LEDs (fig. S33C). The unique mechanical flexibility and stability enable this MSC array to be used in a wearable power system. Figure 6 (A to D) shows a 3 × 9 MSC array attached to a miniaturized robot, which powers a red LED during different actions. When the robot simulates the routine relaxation, bend, stretch, and twist activities of the human body, there is no obvious influence on the brightness of red LED, indicating barrier-free features of the microdevice array in terms of wearable electronics. Besides, various microelectrode patterns are designed and used as both a power supply system and decoration for a bracelet, such as interdigital, parallel lines, and circular arc (fig. S34). There is a reason to prospect that

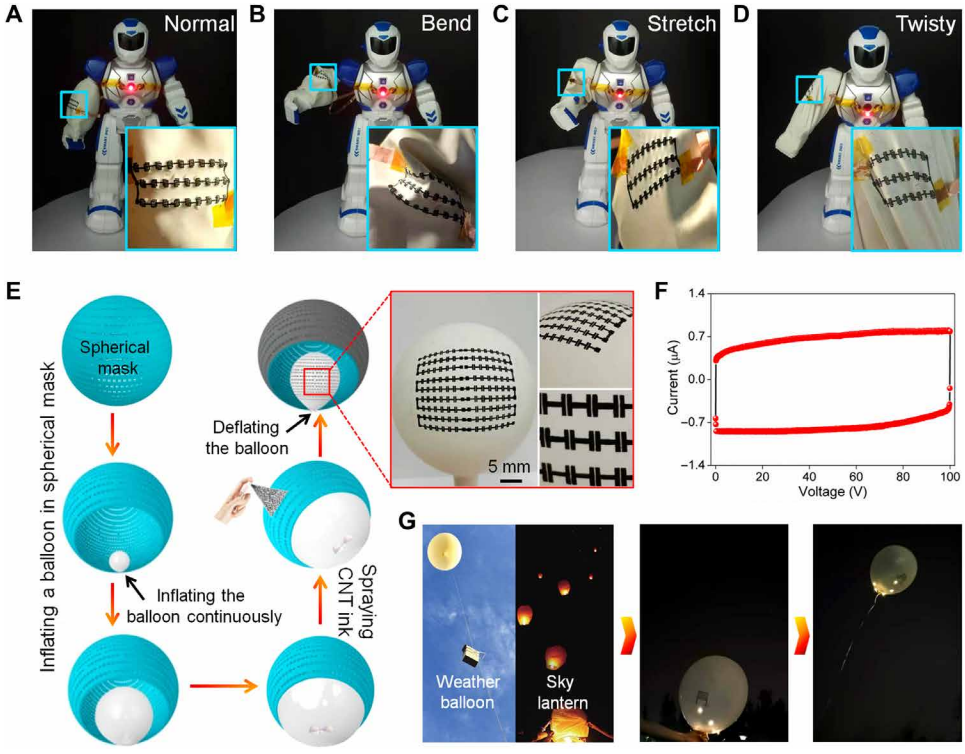

Fig. 6. Diversified application of and spherical integration of MSC array. (**A** to **D**) Integrated MSCs as the wearable power systems in various simulated human motion states. (**E**) Large-scale fabrication of spherical integrated devices and their (**F**) CV curve. (**G**) Schematic diagram of simulation application and demonstration of flight power supply system.

the lightweight, super-flexible balloon-based wearable devices can provide great comfort for the human body. Furthermore, an underwater power supply system has also been developed by pumping moderate amount of water into the balloon containing MSCs, which can be immersed firmly in artificial seawater under internal water pressure and perform normal electrochemical tests without the need for additional electrolyte (fig. S35).

The manufacture of devices on curved surfaces has always been a technical problem, which greatly restricts their diversified applications. Here, on the basis of the balloon elastic substrate, we designed a spherical electrode array mask through 3D printing technology (Fig. 6E and fig. S36). To achieve the fast, large-scale device integration on a spherical surface, a balloon was inflated inside of the mask cavity followed by evenly spraying CNT ink on the mask by using a spray can (Fig. 6E). The whole fabrication process of devices takes less than several seconds. After the ink dried and the balloon shrunk, a large-scale spherical integrated device can be obtained (Fig. 6E and fig. S36E). A small area of 3.9 cm^2 for MSCs connected in series delivers a high voltage of 100 V (Fig. 6F). The spherical integrated devices can be used as a flyable power system to drive a weather balloon or a "green" sky lantern. As displayed in Fig. 6G and fig. S37, the energy storage unit array on the surface of a helium-filled balloon lights a string of LEDs in the sky. Different from the traditional sky lantern, this "electronic lantern" can not only prevent the occurrence of fire but also provide a low-carbon environment. To simulate the low-temperature working environment of the flyable power system in the sky, the electrochemical performance tests of a single crumpled MSC were performed at room temperature, 0° and −10°C (fig. S38, A to C). The capacitance at low temperature decays only a little and maintained stable electrochemical behavior compared with that at room temperature (fig. S38D). Meanwhile, as the altitude increases, the air pressure decreases, causing the balloon to expand in volume. As mentioned in fig. S32, the device array in series still maintains a stable energy output on the surface of the balloon, with dilated strain ranging from 0 to 400%, which further proves the feasibility of the devices as a flyable power system. In addition, in the case of the device used for the power unit in weather balloon, it greatly reduces the dead weight in comparison to the commercial battery (fig. S39), which can keep the balloon flying normally during meteorological detection. Briefly, this fast and facile processing strategy can promote the spherical integrated devices to meet practical industrialization.

DISCUSSION

To sum up, the CNT-based MSC with crumpled microstructures is constructed through a simple omnidirectional elastic contraction induction process. At the state of 80% strain, the MSC has a robust volumetric capacitance of 9.3 F cm^{-3}, superior to the CNT-based microdevices reported previously. Meanwhile, it also holds a high areal capacitance up to 13.5 mF cm^{-2}, which is 45 times greater than that of the initial device (0% strain). Both experiment and theoretical simulation were carried out to investigate the mechanism of performance enhancement, illustrating that the robust charge storage capacity is highly associated with the strain-induced improvements of adsorption energy and conductance for the microelectrodes. In addition, the crumpled microdevices with programmable microelectrode exhibit remarkable conformality and mechanical stability, which can suffer a series of harsh deforming processes, such as bend, knead, prod, and knot. Not only that, we also developed a variety of potential applications such as wearable, underwater, and flyable power systems. By using a customized spherical electrode mask, a scaled device array was integrated on a spherical surface within seconds, which could achieve a high output voltage of 100 V in a small area (3.9 cm^2). Generally, it is the first time to directly prepare MSC with high-precision microstructures through facile contraction strain-induced and screen-printing strategies, which provides a new idea for developing flexible and stretchable in-plane energy storage microdevices with high performance.

MATERIALS AND METHODS

Preparation the electrode masks

A piece of commercial Kapton tape with thickness of 50 μm was first attached to a clean glass plate, and then the electrode masks with desired patterns (interdigital, square, round, and parallel) were fast processed by using a computer-controlled UV laser cutting system (LAJAMIN LASER) with an output power of 5 W. The same method is also applicable to the mask preparation of integrated devices.

Preparation the crumpled MSCs

The patterned electrode mask was transferred to the surface of the inflated balloon. Notably, before the template is transferred, the surface of the inflated balloon needs to undergo a friction process to ensure that the electrode material is uniformly and closely bonded to the balloon substrate by electrostatic interaction. Subsequently, the commercial CNT aqueous ink was spread evenly across the mask by a facile scraping and coating process. The mask was gently torn off after the CNT ink was completely dried at room temperature and atmosphere conditions, and then the interdigital CNT film electrode was obtained. To ensure the good contact between electrode and electrolyte, a thin layer of semisolid electrolyte (1 M H_2SO_4 gel electrolyte) was precoated with the prepared electrode pattern before the balloon deflation. When the balloon contracts, the crumpled MSCs at 20, 40, and 80% contraction strains were obtained. Graphite- and graphene-based crumpled MSCs were also fabricated in the same way as CNT-based MSCs.

Integration of spherical microdevice array

To achieve the fast integration of microdevices on a large scale, a spherical mask with device array pattern was customized by 3D printing technology. A latex balloon was then inflated inside the spherical mask until it completely fills the mask. Next, a spray gun with moderate concentration (diluting the original ink three times) of CNT ink was uniformly sprayed perpendicular to the spherical mask with ~10 s. After the ink dried at room temperature, a spherical microdevice array was obtained through a facile deflation process.

Calculation details

Neo-Hook constitutive relations are used for both the CNT film and balloon substrate with their bulk modulus and Poisson's ratio set to 1000 MPa (10 MPa) and 0.49 (0.49) for the CNT film (balloon substrate).

Finite element method

Both 3D ($25 \times 25 \times 25$ μm^3 and 1-μm thickness) and 2D (100×50 μm^2 and 1-μm thickness) finite element models have been used to study wrinkling phenomenon via ABAQUS. Here, Neo-Hookean bilayer model proposed by Cao and Hutchinson is applied (*18*), and the ratio

of shear modulus of film (50 MPa) and (10 MPa) substrate is set to 5, and Poisson's ratio is 0.49 according to the negligible compressibility observed in the experiments. To accurately describe the wrinkling behavior, the element size is taken approximately 10 times smaller than the wrinkling amplitude. Through defining initial stress, prestretch could be applied on the substrate to reproduce the 500% extension of balloon in experiments. Besides, the out-of-plane displacement field $u_\perp = 0.01 \cdot \cos(k_\perp x_\parallel)$ μm (where $k_\perp$ represents the out-of-plane component of the wave vector and is predicted by using Eq. 1, and $x_\parallel$ is the coordinates parallel to the film plane) at the upper surface is specified as a geometric imperfection. For all FEM calculations, explicit algorithm is adopted, where the loading rate is slow enough to keep kinetic energy less than 0.05% total energy during the whole process.

MD simulation

In our model, CNT is depicted by 10 × 100 coarse-grained particles, which compose a cylinder with 12.8-nm diameter and 400-nm length. According to the previous report (*62*), the total energy of CNT assembly is given as

$$\phi_{tot} = \phi_T + \phi_\varphi + \phi_\theta + \phi_{vdw} \quad (1)$$

where the first three terms are harmonic potentials given by $\phi_T = \frac{1}{2}K_T(r - r_0)^2, \phi_\varphi = \frac{1}{2}K_\varphi(\varphi - \varphi_0)^2, \phi_\theta = \frac{1}{2}K_\theta(\theta - \theta_0)^2$, where the spring coefficients of bonds and angles are K_T = 13,606 kcal/mol per Å^2, $K\varphi$ = 631,829 kcal/mol, and K_θ = 5,706,701 kcal/mol, and the equilibrium distance and angles are taken r_0 = 4 nm, $\varphi_0 = 90°$, and $\theta_0 = 180°$. Besides, van der Waals interaction between CNTs is described via Lennard-Jones potential, i.e., $\phi_{vdw} = 4\varepsilon[(\sigma/r)^{12} - (\sigma/r)^6]$, where ε = 1211 kcal/mol and the equilibrium distance σ = 4 nm. The cross-link between CNTs is included by harmonic potential, which is exactly the same as bond.

Large-scale Atomic/Molecular Massively Parallel Simulator (LAMMPS) was used to perform MD simulations (*39*). The initial configuration of CNT assembly is generated randomly, and then followed by a relaxation. In total, 70% compressive strain is used within 1,400,000 time steps (each time step is set to 20 fs), where NVT (in which the number of particles (N), volume (V) and temperature (T) are fixed) ensemble is used with gradually changing box sizes to simulate the deformation, and the temperature is set to 300 K.

First principles calculation

The adhesion energy between hydrogen atom and graphene is obtained self-consistently by using the projector augmented wave pseudopotential method implemented in the VASP package (*46*), and the exchange-correlation potential is treated by the Perdew-Burke-Ernzerhof (PBE) potential (*47*). In these calculations, 5 × 6 × 1 Monkhorst-Pack meshes is used, 400 eV is chosen for energy cutoff, and less than 1×10^{-5} eV/Å force is asked to reach the structure convergence requirement. According to (*19*), although different exchange-correlation energies give different adhesion energies for hydrogen, the adhesion energy variation with respect to the strain is very similar, demonstrating the robustness of the adhesion energy's strain dependence. For this reason, only PBE exchange correlation potential is used here.

Characterization

SEM (JSM-7001F) was applied to observe the microstructure of prepared devices. UV-vis diffuse reflectance spectroscopy was detected through a UV-vis spectrophotometer (UV2600). A 355-nm UV laser processing system (Beijing Lagamin Laser Co., LM-UVY-5S-Y) was used to fabricate the electrode masks. LAMMPS was used to perform MD simulations. FEM was performed by using ABAQUS. First principles calculation was achieved via the VASP package.

SUPPLEMENTARY MATERIALS

Supplementary material for this article is available at https://science.org/doi/10.1126/sciadv.abn8338

REFERENCES AND NOTES

1. P. Zhang, F. Wang, M. Yu, X. Zhuang, X. Feng, Two-dimensional materials for miniaturized energy storage devices: From individual devices to smart integrated systems. *Chem. Soc. Rev.* **47**, 7426–7451 (2018).
2. Z.-S. Wu, K. Parvez, X. Feng, K. Müllen, Graphene-based in-plane micro-supercapacitors with high power and energy densities. *Nat. Commun.* **4**, 2487 (2013).
3. W. Gao, N. Singh, L. Song, Z. Liu, A. L. M. Reddy, L. Ci, R. Vajtai, Q. Zhang, B. Wei, P. M. Ajayan, Direct laser writing of micro-supercapacitors on hydrated graphite oxide films. *Nat. Nanotechnol.* **6**, 496–500 (2011).
4. Y. Sun, W. M. Choi, H. Jiang, Y. Y. Huang, J. A. Rogers, Controlled buckling of semiconductor nanoribbons for stretchable electronics. *Nat. Nanotechnol.* **1**, 201–207 (2006).
5. C. Yu, C. Masarapu, J. Rong, B. Wei, H. Jiang, Stretchable supercapacitors based on buckled single-walled carbon-nanotube macrofilms. *Adv. Mater.* **21**, 4793–4797 (2009).
6. Y. Huang, M. Zhong, F. Shi, X. Liu, Z. Tang, Y. Wang, Y. Huang, H. Hou, X. Xie, C. Zhi, An intrinsically stretchable and compressible supercapacitor containing a polyacrylamide hydrogel electrolyte. *Angew. Chem. Int. Ed.* **56**, 9141–9145 (2017).
7. Y. Zhou, C. Cao, Y. Cao, Q. Han, C. B. Parker, J. T. Glass, Robust and high-performance electrodes via crumpled Au-CNT forests for stretchable supercapacitors. *Matter* **2**, 1307–1323 (2020).
8. Y. Wang, R. Yang, Z. Shi, L. Zhang, D. Shi, E. Wang, G. Zhang, Super-elastic graphene ripples for flexible strain sensors. *ACS Nano* **5**, 3645–3650 (2011).
9. S.-J. Park, J. Kim, M. Chu, M. Khine, Highly flexible wrinkled carbon nanotube thin film strain sensor to monitor human movement. *Adv. Mater. Technol.* **1**, 1600053 (2016).
10. J. Si, D. Zhong, H. Xu, M. Xiao, C. Yu, Z. Zhang, L.-M. Peng, Scalable preparation of high-density semiconducting carbon nanotube arrays for high-performance field-effect transistors. *ACS Nano* **12**, 627–634 (2018).
11. C. Cao, H. F. Chan, J. Zang, K. W. Leong, X. Zhao, Harnessing localized ridges for high-aspect-ratio hierarchical patterns with dynamic tunability and multifunctionality. *Adv. Mater.* **26**, 1763–1770 (2014).
12. J. Zang, S. Ryu, N. Pugno, Q. Wang, Q. Tu, M. J. Buehler, X. Zhao, Multifunctionality and control of the crumpling and unfolding of large-area graphene. *Nat. Mater.* **12**, 321–325 (2013).
13. P. Kim, M. Abkarian, H. A. Stone, Hierarchical folding of elastic membranes under biaxial compressive stress. *Nat. Mater.* **10**, 952–957 (2011).
14. D. S. Bethune, C. H. Kiang, M. S. de Vries, G. Gorman, R. Savoy, J. Vazquez, R. Beyers, Cobalt-catalysed growth of carbon nanotubes with single-atomic-layer walls. *Nature* **363**, 605–607 (1993).
15. H. Peng, Aligned carbon nanotube/polymer composite films with robust flexibility, high transparency, and excellent conductivity. *J. Am. Chem. Soc.* **130**, 42–43 (2008).
16. X. Sun, T. Chen, Z. Yang, H. Peng, The alignment of carbon nanotubes: An effective route to extend their excellent properties to macroscopic scale. *Acc. Chem. Res.* **46**, 539–549 (2013).
17. K. Xia, J. Fu, Z. Xu, Multiple-frequency high-output triboelectric nanogenerator based on a water balloon for all-weather water wave energy harvesting. *Adv. Energy Mater.* **10**, 2000426 (2020).
18. Y. Cao, J. W. Hutchinson, Wrinkling phenomena in neo-hookean film/substrate bilayers. *J. Appl. Mech.* **79**, (2012).
19. M. Wu, F. Chi, H. Geng, H. Ma, M. Zhang, T. Gao, C. Li, L. Qu, Arbitrary waveform AC line filtering applicable to hundreds of volts based on aqueous electrochemical capacitors. *Nat. Commun.* **10**, 2855 (2019).
20. W. Yu, H. Zhou, B. Q. Li, S. Ding, 3D printing of carbon nanotubes-based microsupercapacitors. *ACS Appl. Mater. Interfaces* **9**, 4597–4604 (2017).
21. H. Kim, J. Yoon, G. Lee, S.-h. Paik, G. Choi, D. Kim, B.-M. Kim, G. Zi, J. S. Ha, Encapsulated, high-performance, stretchable array of stacked planar micro-supercapacitors as waterproof wearable energy storage devices. *ACS Appl. Mater. Interfaces* **8**, 16016–16025 (2016).

22. B. Hsia, J. Marschewski, S. Wang, J. B. In, C. Carraro, D. Poulikakos, C. P. Grigoropoulos, R. Maboudian, Highly flexible, all solid-state micro-supercapacitors from vertically aligned carbon nanotubes. *Nanotechnology* **25**, 055401 (2014).
23. B. Chen, Y. Jiang, X. Tang, Y. Pan, S. Hu, Fully packaged carbon nanotube supercapacitors by direct ink writing on flexible substrates. *ACS Appl. Mater. Interfaces* **9**, 28433–28440 (2017).
24. M. G. Hahm, A. L. M. Reddy, D. P. Cole, M. Rivera, J. A. Vento, J. Nam, H. Y. Jung, Y. L. Kim, N. T. Narayanan, D. P. Hashim, C. Galande, Y. J. Jung, M. Bundy, S. Karna, P. M. Ajayan, R. Vajtai, Carbon nanotube–nanocup hybrid structures for high power supercapacitor applications. *Nano Lett.* **12**, 5616–5621 (2012).
25. J. Lin, C. Zhang, Z. Yan, Y. Zhu, Z. Peng, R. H. Hauge, D. Natelson, J. M. Tour, 3-Dimensional graphene carbon nanotube carpet-based microsupercapacitors with high electrochemical performance. *Nano Lett.* **13**, 72–78 (2013).
26. Y. Yang, L. He, C. Tang, P. Hu, X. Hong, M. Yan, Y. Dong, X. Tian, Q. Wei, L. Mai, Improved conductivity and capacitance of interdigital carbon microelectrodes through integration with carbon nanotubes for micro-supercapacitors. *Nano Res.* **9**, 2510–2519 (2016).
27. J. Ren, L. Li, C. Chen, X. Chen, Z. Cai, L. Qiu, Y. Wang, X. Zhu, H. Peng, Twisting carbon nanotube fibers for both wire-shaped micro-supercapacitor and micro-battery. *Adv. Mater.* **25**, 1155–1159 (2013).
28. M. Beidaghi, C. Wang, Micro-supercapacitors based on interdigital electrodes of reduced graphene oxide and carbon nanotube composites with ultrahigh power handling performance. *Adv. Funct. Mater.* **22**, 4501–4510 (2012).
29. J. Pu, X. Wang, R. Xu, K. Komvopoulos, Highly stretchable microsupercapacitor arrays with honeycomb structures for integrated wearable electronic systems. *ACS Nano* **10**, 9306–9315 (2016).
30. S.-K. Kim, H.-J. Koo, A. Lee, P. V. Braun, Selective wetting-induced micro-electrode patterning for flexible micro-supercapacitors. *Adv. Mater.* **26**, 5108–5112 (2014).
31. L. Liu, D. Ye, Y. Yu, L. Liu, Y. Wu, Carbon-based flexible micro-supercapacitor fabrication via mask-free ambient micro-plasma-jet etching. *Carbon* **111**, 121–127 (2017).
32. F. Wen, C. Hao, J. Xiang, L. Wang, H. Hou, Z. Su, W. Hu, Z. Liu, Enhanced laser scribed flexible graphene-based micro-supercapacitor performance with reduction of carbon nanotubes diameter. *Carbon* **75**, 236–243 (2014).
33. S.-K. Kim, H.-J. Koo, J. Liu, P. V. Braun, Flexible and wearable fiber microsupercapacitors based on carbon nanotube–agarose gel composite electrodes. *ACS Appl. Mater. Interfaces* **9**, 19925–19933 (2017).
34. L. Liu, H.-Y. Li, Y. Yu, L. Liu, Y. Wu, Silver nanowires as the current collector for a flexible in-plane micro-supercapacitor via a one-step, mask-free patterning strategy. *Nanotechnology* **29**, 055401 (2018).
35. J. Yan, C. E. Ren, K. Maleski, C. B. Hatter, B. Anasori, P. Urbankowski, A. Sarycheva, Y. Gogotsi, Flexible MXene/graphene films for ultrafast supercapacitors with outstanding volumetric capacitance. *Adv. Funct. Mater.* **27**, 1701264 (2017).
36. Q. Wang, J. Yan, Y. Wang, T. Wei, M. Zhang, X. Jing, Z. Fan, Three-dimensional flower-like and hierarchical porous carbon materials as high-rate performance electrodes for supercapacitors. *Carbon* **67**, 119–127 (2014).
37. Z. Sun, K. Zhu, P. Liu, Y. Si, H. Li, L. Jiao, Rapid kinetics of Na-ion storage in bimetallic sulfide composite. *Energy Storage Mater.* **41**, 32–40 (2021).
38. Z. Sun, K. Zhu, P. Liu, H. Li, L. Jiao, Optimized cathode for high-energy sodium-ion based dual-ion full battery with fast kinetics. *Adv. Funct. Mater.* **31**, 2107830 (2021).
39. S. Plimpton, Fast parallel algorithms for short-range molecular dynamics. *J. Comput. Phys.* **117**, 1–19 (1995).
40. B. Lu, F. Liu, G. Sun, J. Gao, T. Xu, Y. Xiao, C. Shao, X. Jin, H. Yang, Y. Zhao, Z. Zhang, L. Jiang, L. Qu, Compact assembly and programmable integration of supercapacitors. *Adv. Mater.* **32**, 1907005 (2020).
41. E. Suárez Morell, J. D. Correa, P. Vargas, M. Pacheco, Z. Barticevic, Flat bands in slightly twisted bilayer graphene: Tight-binding calculations. *Phys. Rev. B* **82**, 121407 (2010).
42. S. Reich, J. Maultzsch, C. Thomsen, P. Ordejón, Tight-binding description of graphene. *Phys. Rev. B* **66**, 035412 (2002).
43. F. Liu, C. Wang, Q. Tang, Conductivity maximum in 3D graphene foams. *Small* **14**, 1801458 (2018).
44. F. Teichert, A. Zienert, J. Schuster, M. Schreiber, Improved recursive Green's function formalism for quasi one-dimensional systems with realistic defects. *J. Comput. Phys.* **334**, 607–619 (2017).
45. P. D. Bradford, X. Wang, H. Zhao, Y. T. Zhu, Tuning the compressive mechanical properties of carbon nanotube foam. *Carbon* **49**, 2834–2841 (2011).
46. G. Kresse, J. Furthmüller, Efficient iterative schemes for ab initio total-energy calculations using a plane-wave basis set. *Phys. Rev. B* **54**, 11169–11186 (1996).
47. J. P. Perdew, K. Burke, M. Ernzerhof, Generalized gradient approximation made simple. *Phys. Rev. Lett.* **77**, 3865–3868 (1996).
48. P. L. de Andres, J. A. Vergés, First-principles calculation of the effect of stress on the chemical activity of graphene. *Appl. Phys. Lett.* **93**, 171915 (2008).
49. J. Park, B. Ahn David, J. Kim, E. Cha, B.-S. Bae, S.-Y. Lee, J.-U. Park, Printing of wirelessly rechargeable solid-state supercapacitors for soft, smart contact lenses with continuous operations. *Sci. Adv.* **5**, eaay0764 (2019).
50. J. Bandodkar Amay, S. López Cristian, M. V. M. Allibai, L. Yin, R. Kumar, J. Wang, All-printed magnetically self-healing electrochemical devices. *Sci. Adv.* **2**, e1601465 (2016).
51. J. Zhao, H. Lu, Y. Zhang, S. Yu, I. Malyi Oleksandr, X. Zhao, L. Wang, H. Wang, J. Peng, X. Li, Y. Zhang, S. Chen, H. Pan, G. Xing, C. Lu, Y. Tang, X. Chen, Direct coherent multi-ink printing of fabric supercapacitors. *Sci. Adv.* **7**, eabd6978 (2021).
52. X. Li, H. Li, X. Fan, X. Shi, J. Liang, 3D-printed stretchable micro-supercapacitor with remarkable areal performance. *Adv. Energy Mater.* **10**, 1903794 (2020).
53. G. Lee, J. W. Kim, H. Park, J. Y. Lee, H. Lee, C. Song, S. W. Jin, K. Keum, C.-H. Lee, J. S. Ha, Skin-like, dynamically stretchable, planar supercapacitors with buckled carbon nanotube/Mn–Mo mixed oxide electrodes and air-stable organic electrolyte. *ACS Nano* **13**, 855–866 (2019).
54. D. Qi, Z. Liu, Y. Liu, W. R. Leow, B. Zhu, H. Yang, J. Yu, W. Wang, H. Wang, S. Yin, X. Chen, Suspended wavy graphene microribbons for highly stretchable microsupercapacitors. *Adv. Mater.* **27**, 5559–5566 (2015).
55. L. Li, Z. Lou, W. Han, D. Chen, K. Jiang, G. Shen, Highly stretchable micro-supercapacitor arrays with hybrid MWCNT/PANI electrodes. *Adv. Mater. Technol.* **2**, 1600282 (2017).
56. S. Park, H. Lee, Y.-J. Kim, P. S. Lee, Fully laser-patterned stretchable microsupercapacitors integrated with soft electronic circuit components. *NPG Asia Mater.* **10**, 959–969 (2018).
57. W. Wang, L. Lu, Y. Xie, W. Yuan, Z. Wan, Y. Tang, K. S. Teh, A highly stretchable microsupercapacitor using laser-induced graphene/NiO/Co_3O_4 electrodes on a biodegradable waterborne polyurethane substrate. *Adv. Mater. Technol.* **5**, 1900903 (2020).
58. H. Xiao, Z.-S. Wu, F. Zhou, S. Zheng, D. Sui, Y. Chen, X. Bao, Stretchable tandem micro-supercapacitors with high voltage output and exceptional mechanical robustness. *Energy Storage Mater.* **13**, 233–240 (2018).
59. W. Yan, J. Li, G. Zhang, L. Wang, D. Ho, A synergistic self-assembled 3D PEDOT:PSS/graphene composite sponge for stretchable microsupercapacitors. *J. Mater. Chem. A* **8**, 554–564 (2020).
60. R. Li, L. Li, R. Jia, K. Jiang, G. Shen, D. Chen, A flexible concentric circle structured zinc-ion micro-battery with electrodeposited electrodes. *Small Methods* **4**, 2000363 (2020).
61. Z. H. Guo, M. Liu, Z. Cong, W. Guo, P. Zhang, W. Hu, X. Pu, Stretchable textile rechargeable Zn batteries enabled by a wax dyeing method. *Adv. Mater. Technol.* **5**, 2000544 (2020).
62. S. Cranford, M. J. Buehler, Twisted and coiled ultralong multilayer graphene ribbons. *Modelling Simul. Mater. Sci. Eng.* **19**, 054003 (2011).

Acknowledgments

Funding: This work was supported by the National Key R&D Program of China (2017YFB1104300), NSFC (22075019, 22035005), the National Natural Science Foundation of China (grant nos. 11972349 and 11790292), the Strategic Priority Research Program of the Chinese Academy of Sciences (grant no. XDB22040503), and the Analysis & Testing Center, Beijing Institute of Technology. **Author contributions:** Y.W., Y.Z., F.L., and L.Q. conceived and designed the experiments. Y.W. wrote the paper. Y.H., X.L., and C.D. participated in the characterization of electrochemical performances. X.Z., X.J., and C.S. participated in the discussion of most experimental results. B.L., C.W., and H.C. participated in analyzing the mechanism of electrochemical experiments. **Competing interests:** The authors declare that they have no competing interests. **Data and materials availability:** All data needed to evaluate the conclusions in the paper are present in the paper and/or the Supplementary Materials.

Submitted 23 December 2021
Accepted 11 April 2022
Published 27 May 2022
10.1126/sciadv.abn8338